Journal of Controlled Release xxx (2016) xxx–xxx

Contents lists available at ScienceDirect

Journal of Controlled Release

journal homepage: www.elsevier.com/locate/jconrel

The role of subcutaneous tissue stiffness on microneedle performance in a representative in vitro model of skin

K. Moronkeji [a], S. Todd [b], I. Dawidowska [b], S.D. Barrett [c], R. Akhtar [a,*]

[a] Centre for Materials and Structures, School of Engineering, University of Liverpool, L69 3GH, United Kingdom
[b] Renephra Ltd., MedTech Centre, Manchester Science Park, Pencroft Way, M15 6JJ, United Kingdom
[c] Department of Physics, University of Liverpool, L69 7ZE, United Kingdom

ARTICLE INFO

Article history:
Received 27 July 2016
Received in revised form 14 October 2016
Accepted 8 November 2016
Available online xxxx

Keywords:
Microneedles
Impact testing
Neonatal porcine skin
Stratum corneum
Penetration
Nanoindentation
Gelatine gels
Perma-Gel®

ABSTRACT

There has been growing interest in the mechanical behaviour of skin due to the rapid development of microneedle devices for drug delivery applications into skin. However, most in vitro experimentation studies that are used to evaluate microneedle performance do not consider the biomechanical properties of skin or that of the subcutaneous layers. In this study, a representative experimental model of skin was developed which was comprised of subcutaneous and muscle mimics. Neonatal porcine skin from the abdominal and back regions was used, with gelatine gels of differing water content (67, 80, 88 and 96%) to represent the subcutaneous tissue, and a type of ballistic gelatine, Perma-Gel®, as a muscle mimic. Dynamic nanoindentation was used to characterize the mechanical properties of each of these layers. A custom-developed impact test rig was used to apply dense polymethylmethacrylate (PMMA) microneedles to the skin models in a controlled and repeatable way with quantification of the insertion force and velocity. Image analysis methods were used to measure penetration depth and area of the breach caused by microneedle penetration following staining and optical imaging. The nanoindentation tests demonstrated that the tissue mimics matched expected values for subcutaneous and muscle tissue, and that the compliance of the subcutaneous mimics increased linearly with water content. The abdominal skin was thinner and less stiff as compared to back skin. The maximum force decreased with gel water content in the abdominal skin but not in the back skin. Overall, larger and deeper perforations were found in the skin models with increasing water content. These data demonstrate the importance of subcutaneous tissue on microneedle performance and the need for representative skin models in microneedle technology development.

1. Introduction

Skin is a complex organ made up of the epidermis, dermis and hypodermis with the intrinsic function of protecting the body from physical and environmental assaults [1]. Skin exhibits complex mechanical behaviour as it is subjected to pre-stress and exhibits anisotropic [2,3], non-linear [4] and viscoelastic [5,6] behaviour. These properties are influenced by elastin, proteoglycans, collagen and interstitial fluid [7,8] and vary with a number of factors including age [9,10], anatomical site [11], and level of hydration [12]. The dermal layer governs the general mechanical behaviour of skin, however, contribution from the uppermost layer of skin, the stratum corneum on the global behaviour of skin is also important. The stratum corneum is the stiffest of the skin's layers and affects strain magnitude and direction in the underlying layers [13]. It also exhibits less viscoelastic behaviour as compared to other layers [14].

There has been growing interest in the mechanical behaviour of skin due to the development of micro-devices for drug delivery into upper layers of skin [15]. The use of microneedle arrays for transdermal drug application is gaining in popularity in the pharmaceutical industry [16]. This is because it is a painless method of delivering vaccines or therapeutic compounds via skin [17]. One of the benefits of the insertion of numerous sub-millimetre needle projections on a base substrate to skin is that it causes little damage to the stratum corneum [18,19] in order to access the epidermal layer. Typically, the microneedles are not designed to travel beyond the epidermis to the dermis where nerve endings may be stimulated or blood vessels damaged. Hence, minimal or no pain or bleeding occurs to the patient following application. Despite significant advances in the field of microneedles, the complexity of the mechanical behaviour of skin coupled with the inherent elasticity of the stratum corneum [20] still poses some challenges for microneedle application.

* Corresponding author at: Centre for Materials and Structures, School of Engineering, University of Liverpool, L69 3GH, United Kingdom.
E-mail address: r.akhtar@liverpool.ac.uk (R. Akhtar).

http://dx.doi.org/10.1016/j.jconrel.2016.11.004

Currently, there are a huge range of different microneedle arrays that have been developed and the needles vary greatly in terms of geometry, material, length and spacing. Hence, for most studies in vitro experimentation is vital for determining microneedle performance for a particular array, for a number of factors, including for regulatory purposes. However, to date the methodology used for testing microneedles on animal skin or human skin explants is both variable and unrepresentative of the mechanical environment of skin in vivo. For example, previous studies have used a filter paper soaked in phosphate buffered saline (PBS) solution supported by cork plates [21] [21], dental wax [22], clay [23,24], soft sponge pad [25], ten layers of tissue paper [26] and Styrofoam support [27] as underlying substrates of skin. All of these approaches appear to be arbitrary methods of representing skin sub-layers. The role of subcutaneous layers on microneedle performance is important from a biomechanical perspective. However, this area has largely been unexplored and may be important for some medical conditions such as oedema. As such, it may be difficult to reliably predict the response of skin in relation to subcutaneous properties following microneedle application. In this study, we aimed to develop a representative in vitro skin model to determine the response of the skin model following application of dense polymethylmethacrylate (PMMA) microneedle arrays. By altering the physical properties of the skin model, we explore the role of both skin stiffness and subcutaneous layers on microneedle performance. By using a custom impact test setup we were able to quantitatively determine the insertion force and velocity required for successful penetration of the needles in to skin.

2. Materials and methods

All the chemicals used in this study were obtained from Sigma-Aldrich (Dorset, UK) unless otherwise stated.

2.1. In vitro skin model

All experimental testing was conducted using neonatal porcine skin due to its biomechanical properties being similar to human skin [28] and for ease of availability. The in vitro skin model was made up of neonatal porcine skin as the top layer, gelatine gel as the second layer, representing the subcutaneous layer and Perma-Gel® as the lowermost layer representing muscle, as shown in Fig. 1. The skin model was secured in mechanical clamps prior to testing.

2.1.1. Neonatal porcine tissue

Three fresh suckling pigs (7–10 weeks old) were obtained from a local abattoir. Skin samples from the back and abdomen were dissected within 3–4 h and immediately snap-frozen by placing in super-cooled isopentane. These were subsequently stored at −80 °C until required. Prior to testing, the skin tissue was de-thawed for 30 min. Commercial hair removal cream for normal skin (Veet, Reckitt Benckiser Group, Berkshire, UK) was applied to the skin surface for 5 min to remove any hair. The samples were kept hydrated in phosphate buffered saline (PBS) solution during testing.

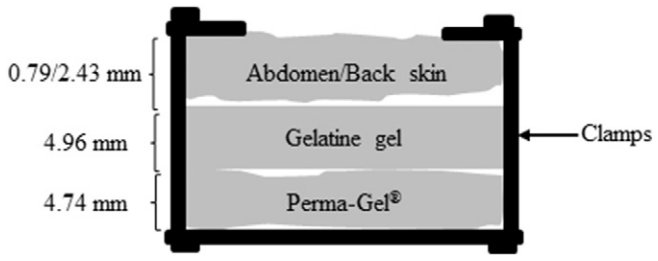

Fig. 1. The layers of the in vitro skin model. The thickness of the abdomen and back skin was 0.79 mm and 2.43 mm respectively.

2.1.2. Gelatine gels

Several factors such as gel preparation, curing duration, cooling and measurement temperatures can influence the elastic and shear moduli of gelatine gels [29]. Hence, each gel concentration was prepared in a consistent manner with the following concentrations: 67, 80, 88, 96% water content by weight. Each gel solution was left to cool for 1 h, before it was cured at 5 °C for 4–5 h. All tests were carried out within 2 h.

2.1.3. Perma-Gel®

Perma-Gel®, (Perma-Gel®, Inc., Albany, OR), which is similar to ballistic gelatine, is used as muscle mimic [30] and a general tissue surrogate [31]. An advantage of Perma-Gel® over ballistic gelatine is that it can be used at room temperature whereas ballistic gelatine has to be used at 4 °C or lower. It has many of the same characteristics as 10% ballistic gelatine [32,33]. Perma-Gel® was obtained in block form (445 mm × 292 mm × 127 mm) from a third party distributor (MidwayUSA, Columbia, USA). The Perma-Gel® was cut in to small specimens to fit the mechanical clamps. Synthetic thermoplastic materials such as Perma-Gel® are stable at room temperature and can be stored for long periods of time [32].

2.2. Microneedle Array

Dense Polymethylmethacrylate (PMMA) microneedle arrays were used for all experiments (10x technology, IL, USA), with the full specifications for these microneedles presented in Table 1.

2.3. Dynamic nanoindentation tests

All dynamic nanoindentation experiments were carried out on gelatine gels, Perma-Gel® and fresh full thickness skin samples. During testing, the tissue was kept hydrated in PBS solution. Testing was not possible on the 96% gelatine gel due to its extremely high compliance. Nanoindentation tests were conducted using a Keysight Technologies Nanoindenter G200 (Chandler, AZ, USA) instrument with an ultra-low load dynamic contact module indentation head (DCM-II actuator). The indentations were performed at ambient temperature (24.3–27.2 °C) using a 100 μm indenter tip (Synton-MDP Ltd., Nidau, Switzerland). A custom sample holder was designed in to which the gel samples were placed. The well in the sample holder was 1 cm^2 and 4 mm deep.

The DCM-II actuator was used to perform dynamic (oscillatory) indentation as per our previous studies [34,35]. The method allows the determination of the complex shear modulus (G^*), which exhibits real and imaginary components and gives the intrinsic elastic (G') and viscous (G'') properties of the material, (Eq.(1)):

$$G* = G\prime + iG'' \tag{1}$$

where G' and G'' represent the shear storage modulus and shear loss modulus respectively. The theoretical basis for this method has been covered in detail elsewhere [34].

For the experiments conducted in this study a pre-compression of 5 μm for the gelatine gels and Perma-Gel® was selected, whilst 8 μm was used for the skin samples. The indenter was vibrated at a frequency of 110 Hz (the resonant frequency of the indenter) and with an oscillation amplitude of 500 nm. The surface detection relied on a phase shift of the displacement measurement as outlined previously [34]. 10 different sites were tested on each sample.

The Poisson's ratio (ν) of skin was assumed to be 0.5, based on previous studies in the literature [36], and was used to estimate the elastic modulus (E):

$$G\prime = \frac{E}{2(1+\nu)} \tag{2}$$

Please cite this article as: K. Moronkeji, et al., The role of subcutaneous tissue stiffness on microneedle performance in a representative in vitro model of skin, J. Control. Release (2016), http://dx.doi.org/10.1016/j.jconrel.2016.11.004

Table 1
PMMA microneedles specification.

Type	Height (μm)	Disc size diameter (mm)	Needles per unit area (mm^2)	Base (μm)	Centre-to-centre spacing (μm)	No. of needles per array
Polymeric	552	30.1	7.7	160	360	>6000

2.4. Impact tests for microneedle application

A custom dropped weight impact testing rig was used to insert the microneedles into the skin model. It was comprised of a drop tower of height 1.86 m, with a drop tower guide of height 1.78 m, a piezoelectric accelerometer with 10.71 mV/g sensitivity (Model 3225F-1, Dytran Instruments, Inc., CA, USA) and a piezoelectric force transducer with 22.4 mV/N sensitivity (Model 1022V, Dytran Instruments, Inc., CA, USA). Both the accelerometer and the transducer were connected to their respective amplifiers and to a digital oscilloscope (54641A, Keysight Technologies, Berkshire, UK) and controlled with a Keysight IntuiLink software (Version 3.1). The accelerometer was connected to the top of a custom-made 36 g drop mass, whilst the force transducer was fastened to its bottom end. Two 630–650 nm wavelength (red) with a power output <1 mW laser diode modules (PL-Series, Hero Electronics, Dunstable, UK) were attached to two drill holes on the lower part of the drop tower guide so that a break in signal, caused when the drop mass is released, was captured by a beam detector, thus activating the external trigger on the oscilloscope. Following this, the force and acceleration outputs were captured on the oscilloscope. The rig has been described in detail previously [37].

Prior to testing, the microneedle array was placed on the clamped skin model. The drop mass was then released from a height of 0.46 m equivalent to a nominal velocity of 3 ms^{-1} along the length of the drop tower guide to impact the microneedles at the bottom of the drop tower guide. This height/velocity was selected following calibration experiments which are presented in Supplementary Data (Fig. S1). The drop mass was released once for each skin model i.e. abdominal and back regions with gelatine gels of differing water content (67, 80, 88 and 96%) and Perma-Gel®. 5 repeats were carried out for each model. Typical velocity-time and force-time plots are shown in Fig. 2.

The force and velocity values for each test were extracted from these plots. Due to the high impact velocity used in our experimental setup, it is difficult to precisely determine the exact moment that the microneedles penetrated through the skin. However, due to the characteristics of the plots shown in Fig. 2, the insertion force and insertion velocity could be inferred. Calibration data with the impact test setup is presented in the Supplementary Data (Fig. S2). The maximum values for force and velocity are presented throughout the paper. The highly elastic nature of skin is evident from the displacement-time plot shown in Fig. 2c. Once the drop mass makes contact with skin, there is around 4 mm of deformation of the model. Following this, some elastic recovery is evident. In order to account for the elastic recovery of skin and to ensure that the microneedles were fully embedded in the skin [39], the microneedles were left in the skin for approximately 2 min prior to removal for subsequent imaging.

All impact tests were conducted at ambient temperature, which was ideal for maintaining the stability of the gels used in the models.

2.5. Imaging of microneedle penetration quality

2.5.1. Methylene blue staining

2% methylene blue solution was used to detect whether any microchannels were created in the skin following impact tests. The

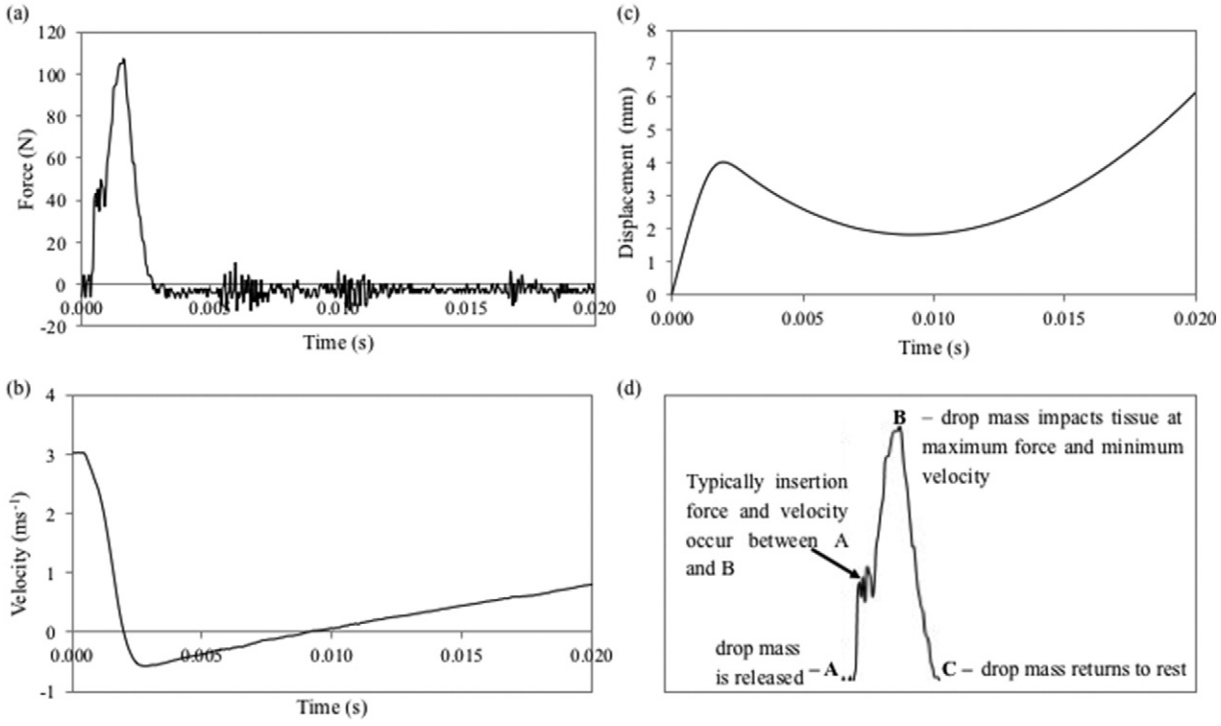

Fig. 2. Impact tests of tall microneedles on a back skin model with 88% water content, where (a) force–time plot (b) velocity–time plot (c) displacement–time plot and (d) the description of points along the force–time curve. The impact occurred at 0.9 ms, where the velocity was approximately 2.5 ms^{-1}, the force was 37.1 N and the maximum force reached was 103 N. The data suggest that the initial insertion occurred at 0.9 ms. Hence, at this point the velocity was approximately 2.5 ms^{-1}, the force was 37.1 N and the maximum insertion velocity and force reached were 3 ms^{-1} and 103 N respectively. In the absence of any microneedles, a smooth force-time plot up to the maximum load would be expected for a drop mass impacting on a tissue sample [38].

Please cite this article as: K. Moronkeji, et al., The role of subcutaneous tissue stiffness on microneedle performance in a representative in vitro model of skin, J. Control. Release (2016), http://dx.doi.org/10.1016/j.jconrel.2016.11.004

microneedle treated tissue was soaked in methylene blue solution for 30 min. The tissue was removed from the methylene blue solution and the tissue surface wiped down with ethanol so that any microchannels were detected. The staining occurs because the methylene blue dye binds itself to the proteins that exist in tissue [40]. The image of the methylene blue staining indicates successful breach of the stratum corneum and the creation of microchannels on the skin. Typically, the hydrophobic nature of the stratum corneum cannot absorb the hydrophilic low molecular weight of the methylene blue solution, however, once the stratum corneum has been disrupted by the microneedles, the methylene blue diffuses through the skin [41]. The skin samples were imaged with Nikon digital camera D5100 (Surrey, UK), as shown in Fig. 3.

Due to the size of the microneedle arrays used in this study (30.1 mm diameter) and the density of microneedles (>6000), it was difficult to reliably quantify the penetration efficiency following methylene blue staining for the entire disc. Hence, for quantitative analysis, a central region (5 × 5 mm) was cropped for each image (Fig. 3b) and this was used for determining the penetration efficiency using a method similar to that of van der Maaden et al. [42]. In our case, penetration efficiency (PE) was calculated as follows:

$$PE = \frac{number\ of\ blue\ spots}{193} \times 100\% \quad (3)$$

where 193 represents the expected number of microneedles for a 25 mm^2 area of the sample given the 7.7 needles per mm^2 microneedle density reported by the manufacturer.

2.5.2. Haematoxylin and eosin staining

After impact testing, the tissue was prepared for cryosectioning by freezing in Optimal Cutting Temperature (OCT) resin (Sakura Fintek Europe B.V, Alphen aan den Rijn, The Netherlands) and then immediately frozen in super-cooled isopentane [43]. Histological evaluation using haematoxylin and eosin (H&E) staining was useful in this study for assessing the depth of the microchannels created within skin. The skin was processed by fixation in 4% paraformaldehyde followed by rehydration in a series of alcohol baths. It was subsequently stained with H&E. The stained tissue was then sectioned to 12 μm thickness using a Leica CM1850 cryostat (Milton Keynes, UK) and imaged with a Nikon Eclipse Ci microscope (Surrey, UK). Example images following H&E staining before and after hair removal treatment are shown in Fig. 4. No adverse effects on skin histology were recorded as a result of the hair removal.

2.5.3. X-ray micro computed tomography (XMT) imaging

X-ray Micro Computed Tomography (XMT) is a powerful method for non-invasive imaging of soft tissue. XMT is a high resolution imaging technique that has gained wide use within the scientific community [44]. Traditionally, XMT has been predominantly used for the imaging of bone structures [45]. The challenge with XMT of soft tissue is as a result of its low inherent X-ray contrast [46,47]. The use of contrast agents on soft tissue can overcome this limitation. XMT imaging was used to validate the measurements obtained with histological imaging on an abdominal skin model with 88% gel water content. XMT was conducted in this study to characterize the topography of the skin and also to validate the breach areas observed with H&E staining. The testing was conducted on an abdominal skin model with 67% water content.

In order to conduct XMT imaging, a staining protocol was conducted to discriminate the different histological layers of skin and enhance the contrast. This protocol is summarized here. Following impact testing, the microneedles were left embedded in the skin for 2 min before removal. The full thickness microneedle treated skin was soaked in paraformaldehyde for 4 h and then rehydrated in phosphate buffered saline (PBS) solution for 5 min. The tissue was then subsequently stained with Lugol's contrasting agent for 21 h. Following on from the staining, the sample was washed three times in water and placed in 70% ethanol for 15 min, then in 90% IMS for 15 min, followed by 15 min in 100% ethanol and then 3 xylene washes of 30 min. Finally, it was placed on the processor for wax embedding for 30 min. After wax embedding, the sample was trimmed to approximately 2 mm × 2 mm.

The skin was imaged on a Carl Zeiss Xradia MicroXCT-500 system using 4× objective, with a source voltage of 45 kV, a source current of 78 μA and a power source of 3.5 W. The sample was positioned 8 mm from the source and 45 mm from the detector.

From the XMT imaging, 1015 TIFF images were obtained using Avizo 8 imaging software (FEI™, Oregon, USA). The image stacks were opened in ImageJ using the orthogonal selection. The XY view showed the vertical cross-section of the skin through the stratum corneum, epidermis and dermis, whilst the XZ view showed the planar cross-section of the skin through the dermis. The orthogonal views are shown in

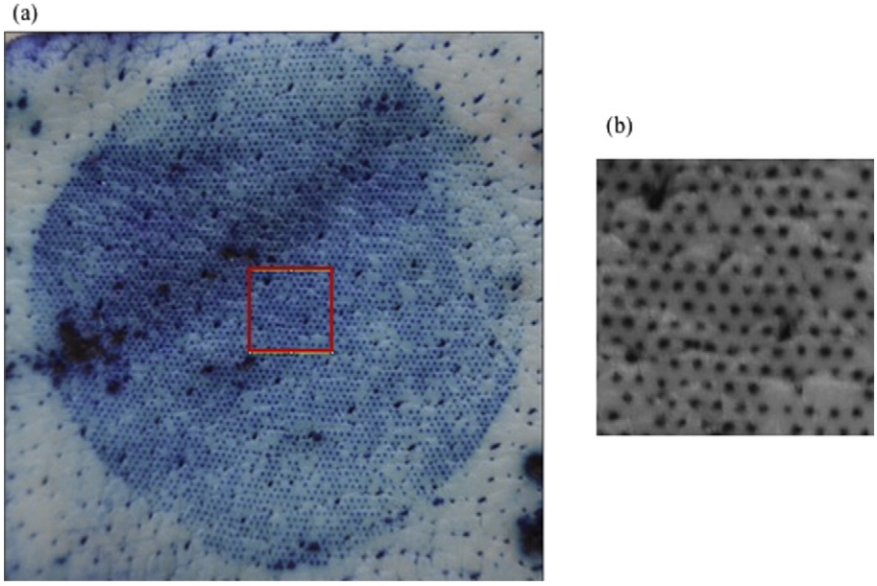

Fig. 3. Inspection technique of skin for penetration efficiency with methylene blue staining where (a) shows the whole disc which provided visual confirmation of penetration. (b) Cropped image showing region highlighted in (a). The cropped region is 5 × 5 mm and was used for calculating penetration efficiency. (For interpretation of the references to colour in this figure legend, the reader is referred to the web version of this article.)

Please cite this article as: K. Moronkeji, et al., The role of subcutaneous tissue stiffness on microneedle performance in a representative in vitro model of skin, J. Control. Release (2016), http://dx.doi.org/10.1016/j.jconrel.2016.11.004

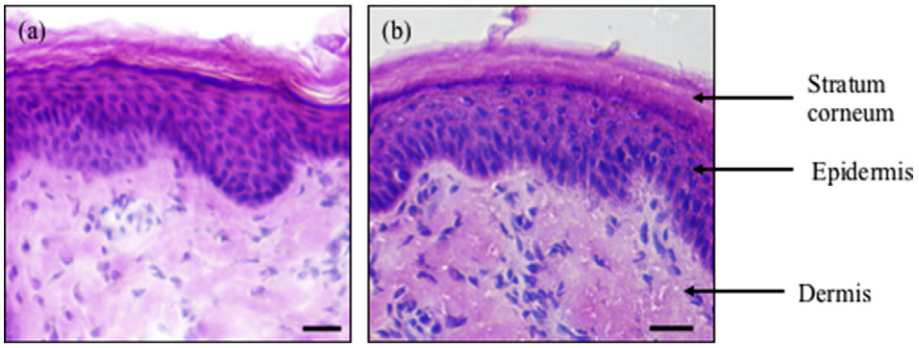

Fig. 4. H&E staining of the sectioned tissue (a) treated with the hair removal agent and (b) untreated sectioned tissue showing the three histological layers of skin. Scale bar represents 100 μm.

Supplementary Information Fig. S3. Fig. S4 shows that the different histological layers of the skin were visible in the XMT images. Comparison of H&E and XMT images is shown in Fig. S5.

The 3D reconstruction of the image stacks was carried out using Avizo 8 (FEI, Oregon, USA) and prior to segmentation, noise in the data was reduced by applying a non-local means filter.

2.5.4. Image analysis

2.5.4.1. Depth of penetration. ImageJ (Version 1.48, National Institutes of Health, MD, USA) was used to assess the perforation depth of the histology image. In ImageJ, the selection was a user-defined line within the image. The user-defined line was created using the straight line selection tool. The length of the line selections was used to measure the perforation depth in the histology image. This was done for over 30 histology images selected at random per skin model. The user-defined line was drawn from the stratum corneum to the maximum point of penetration in the skin, which was either located within the epidermis or the dermis (Supplementary Information Fig. S4).

2.5.4.2. Breach area. A custom routine was written in Image SXM [48] for semi-automated analysis of the histology images to determine the breach area within the skin following microneedle application. The optical microscopy images were found to vary in contrast, brightness and colour balance and hence a histogram of pixel values was used to determine the optimum threshold in order to highlight the pixels above the epidermal layer. For images in which the epidermal layer had not been breached, it was found that combining the red and blue colour channels of the images produced the most reliable discrimination of the edge of the epidermal layer. For images in which the epidermal layer was breached, it was found that the green channel gave the most reliable discrimination. Automatic detection of a breach was not possible with the routine; hence the most appropriate mode was selected for each image. Only those images in which the epidermal layer was clearly discriminated from the rest of the image could be analysed to determine the breach area. For these images, the extent of the microneedle puncture was marked by clicking on the two points (Fig. 5a) that delineate the puncture at the upper surface of the epidermal layer (Fig. 5b). The area of the puncture was measured and logged (Fig. 5c). Subsequently, the next image was loaded and displayed ready for user input. Over 200 images were analysed in this manner.

For analysis, the breach areas were grouped into three categories; 0 < breach area < 10,000 μm^2, 10,000 < breach area < 20,000 μm^2 and 20,000 < breach area < 50,000 μm^2 (Fig. 6).

2.5.5. Statistical analysis

The nanoindentation data are presented as mean ± standard deviation (SD). The penetration depth and breach area are presented as the geometric mean and geometric standard deviation (geoSD) due to the skewed nature of the distribution.

3. Results

3.1. Micromechanical properties of the different layers of the skin model

The micromechanical properties for the skin and gels is summarized in Table 2. Of all the layers in the skin model, the Perma-Gel® had the highest elastic component, whilst the 88% gelatine gel concentration had the lowest elastic component. Back skin had the highest viscous component, whilst the 88% gelatine gel concentration had the lowest viscous component. Abdominal skin exhibited the highest damping capacity, whilst Perma-Gel® had the lowest damping capacity, as determined from the loss factor.

The back skin had a significantly higher elastic modulus as compared to the abdominal skin samples. However, the abdominal skin had a significantly higher loss factor as compared to the back skin, as the loss

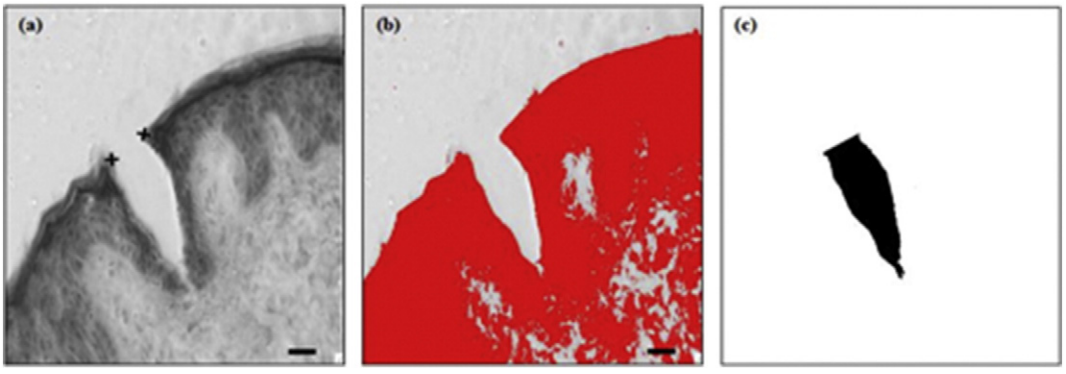

Fig. 5. Image analysis routine: (a) Histology image in grayscale used for analysis where the microneedle breach is clearly visible. (b) Thresholded image following user demarcation of the edges of the breach (c) Area of the breach used for analysis.

Please cite this article as: K. Moronkeji, et al., The role of subcutaneous tissue stiffness on microneedle performance in a representative in vitro model of skin, J. Control. Release (2016), http://dx.doi.org/10.1016/j.jconrel.2016.11.004

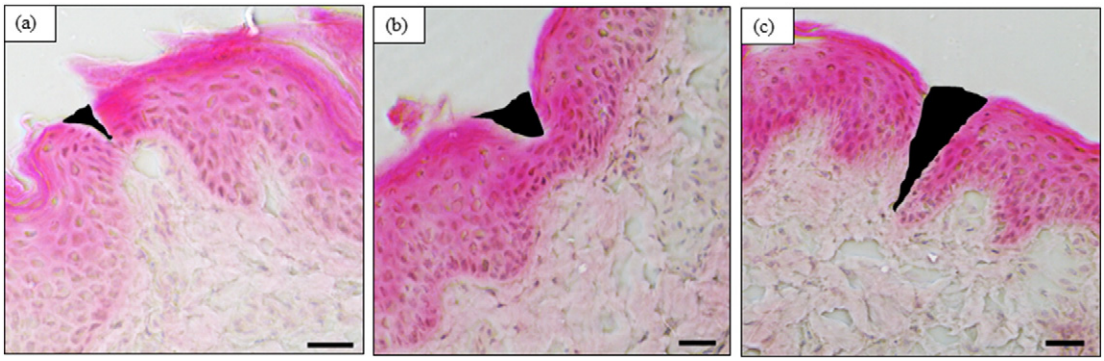

Fig. 6. H&E images which illustrate breach area groupings. The area shaded in black represents the breach area size, where (a) The area is > 0 ≤ 10,000 μm^2 (b) > 10,000 ≤ 20,000 μm^2 i.e. a large deformation within the epidermis and (c) > 20,000 ≤ 50,000 μm^2. Scale bar represents 100 μm.

modulus (G″) dominated over the storage modulus (G′). In contrast, G′ was higher than G″ for the back skin.

With increasing water content, the elastic modulus decreased for the gelatine gels in a linear fashion as shown in Fig. 7. G′ and G″ both decreased with increasing water content. The damping factor also decreased with increasing water content.

3.2. Force

The insertion force which was inferred from the force-time plots (Fig. 2a) did not vary with gel concentration, but was approximately 10 N higher for most of the back skin models as compared to the abdominal skin models (Fig. 8a). Fig. 8b shows the variation of the maximum force across the different abdominal skin models. The maximum force decreased progressively with increasing water content of the subcutaneous mimic. This was found to be related to the elastic modulus of these gels (Fig. 8c). For the back skin, the maximum force was relatively constant for all gel concentrations except for the 88% back skin model (67%–102 N; 80%–100 N; 88%–46 N; 96%–102 N). At 67%, there was no difference in the maximum force with the two different types of skin i.e. the thicker and stiffer back skin did not require a larger insertion force. The difference in the force values in the two skin models was much more pronounced at the higher water contents.

3.3. Microneedle penetration as a function of water content in the skin models

Fig. 9 demonstrates that overall successful microneedle penetration occurred in all of the skin models.

The penetration efficiency results decreased with increasing water content for the abdomen skin but a similar trend was not seen with the back skin. As expected, 100% penetration efficiency was not achieved. This is likely due to the inherent topography of the skin, as characterised in 3D with the XMT imaging (Fig. 10).

Although the methylene blue staining provided quick visual confirmation that the majority of the microneedles had successfully penetrated the stratum corneum, the H&E images were necessary to understand the penetration profile of the microneedles in each of the skin models.

Table 2
Micromechanical properties of the different components of the skin models.

Sample	G′ (kPa) ± SD	G″ (kPa) ± SD	E (kPa) ± SD
Abdomen skin	8.2 ± 1.8	10.0 ± 1.9	24.5 ± 5.5
Back skin	15.3 ± 3.2	10.7 ± 2.7	45.9 ± 9.6
67% Gel	21.0 ± 2.1	3.8 ± 0.2	63.1 ± 6.2
80% Gel	11.5 ± 1.1	2.0 ± 0.4	34.6 ± 3.2
88% Gel	3.8 ± 0.6	0.9 ± 0.3	11.3 ± 1.6
Perma-Gel®	26.9 ± 0.9	2.7 ± 0.8	80.7 ± 2.7

Furthermore, as abdominal tissue is typically thinner than back tissue, for both tissues the microneedles appeared to fully open up the epidermis. However, in many cases the breach in the abdominal tissue travelled deeper into the skin, to the dermis, whereas the deformation within the back tissue was wider and predominantly contained within the epidermis. Qualitative assessment of the images also suggested that there was more deformation in the models with higher water content (Fig. 11). The exception appeared to be the 88% back skin model where less deformation was visible as compared to the models with less water content.

The depth of penetration for each of the skin models is shown in Fig. 12. For the abdominal skin (Fig. 12a), the depth of penetration increased with gel water content but was lowest for the 96% gel. For the back skin, the depth of penetration was lower at each gel concentration relative to the abdominal skin except at 96%. Values for the 88% back skin model were much lower following the trends observed with the insertion force data and qualitative assessment of the H&E images.

The overall trends in the breach area as determined by the geometric mean are shown in Fig. 13. The trends followed those for penetration depth (shown in Fig. 12).

With the abdominal skin models, over 70% of the measured perforations had an area < 10,000 μm^2 for the model with the lowest water content gel. This was also the case for the gel with the highest water content. The difference between the 67% gel model and the others was the much larger percentage of perforations >20,000 μm^2. These trends are shown in Fig. 14a. A similar pattern was seen with the back skin models. Although there were lower perforation areas <

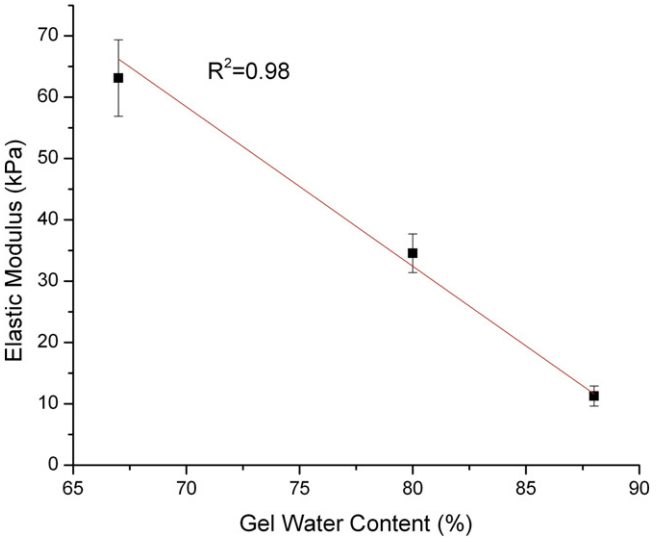

Fig. 7. Linear relationship between elastic modulus and gel water content.

Please cite this article as: K. Moronkeji, et al., The role of subcutaneous tissue stiffness on microneedle performance in a representative in vitro model of skin, J. Control. Release (2016), http://dx.doi.org/10.1016/j.jconrel.2016.11.004

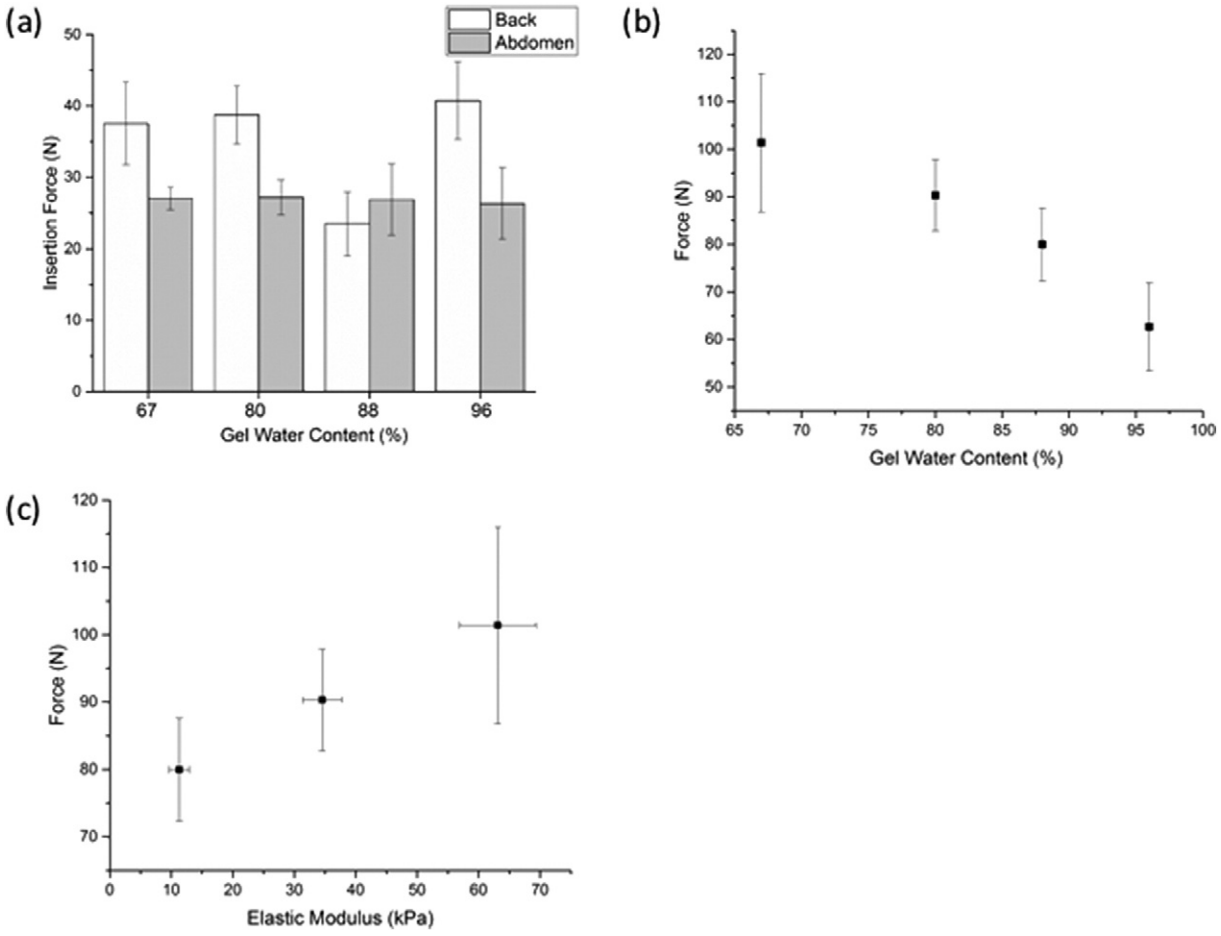

Fig. 8. Force data (a) Insertion force data for the back and abdominal skin models (b) Maximum force vs gel water content for abdomen skin models (b) Maximum force for the abdomen skin models vs elastic modulus of the gelatine gels.

10,000 μm^2 in the 80% model (40%), there was a much larger percentage of perforations >20,000 μm^2 (Fig. 14b).

4. Discussion

The subcutaneous layers play an important role in the mechanical properties of skin. In the body, subcutaneous adipose tissue contributes to skin deformation during loading and load transfer from skin to deeper layers [49]. However, the role of subcutaneous tissue on microneedle performance has largely been ignored due to inadequate in vitro skin models. Our study demonstrates that, in a representative skin model, the role of the subcutaneous layer is important for determining microneedle performance. Our study utilized impact testing to apply microneedles to the skin models in vitro. Impact testing was selected as it allows a reproducible method of microneedle application with quantification of the insertion velocity and force. We also quantified the mechanical properties of the various layers of the model and related these to the microneedle performance.

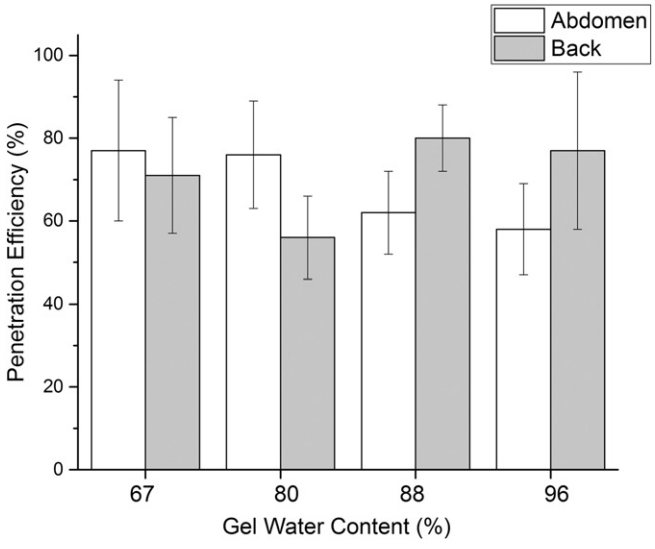

Fig. 9. Penetration efficiency determined from the methylene blue images.

4.1. Micromechanical properties of the skin model layers

Nanoindentation allowed characterization of the different layers of the skin models and thereby comparison with values reported in the literature for subcutaneous and muscle tissue. Our measurements on Perma-Gel® yielded a mean G′ of 29.9 ± 0.9 kPa which matches values reported in the literature for the shear modulus of muscle [50]. For subcutaneous tissue, G′ of 7.5 kPa has been reported in the literature for porcine tissue [51]. For our gelatine gels, G′ ranged from 3.8–21 kPa. These are also comparable given the much higher frequency that our testing was carried out at (110 Hz as compared to approximately 1.6 Hz in the rheology study by Geerligs et al. [51]).

The micromechanical tests on three concentrations of gelatine gels showed that the elastic modulus decreased in a linear fashion with increasing fluid content in the gelatine gels matching trends reported by Mridha et al. [52,53]. By varying the properties of these gels, the role

Please cite this article as: K. Moronkeji, et al., The role of subcutaneous tissue stiffness on microneedle performance in a representative in vitro model of skin, J. Control. Release (2016), http://dx.doi.org/10.1016/j.jconrel.2016.11.004

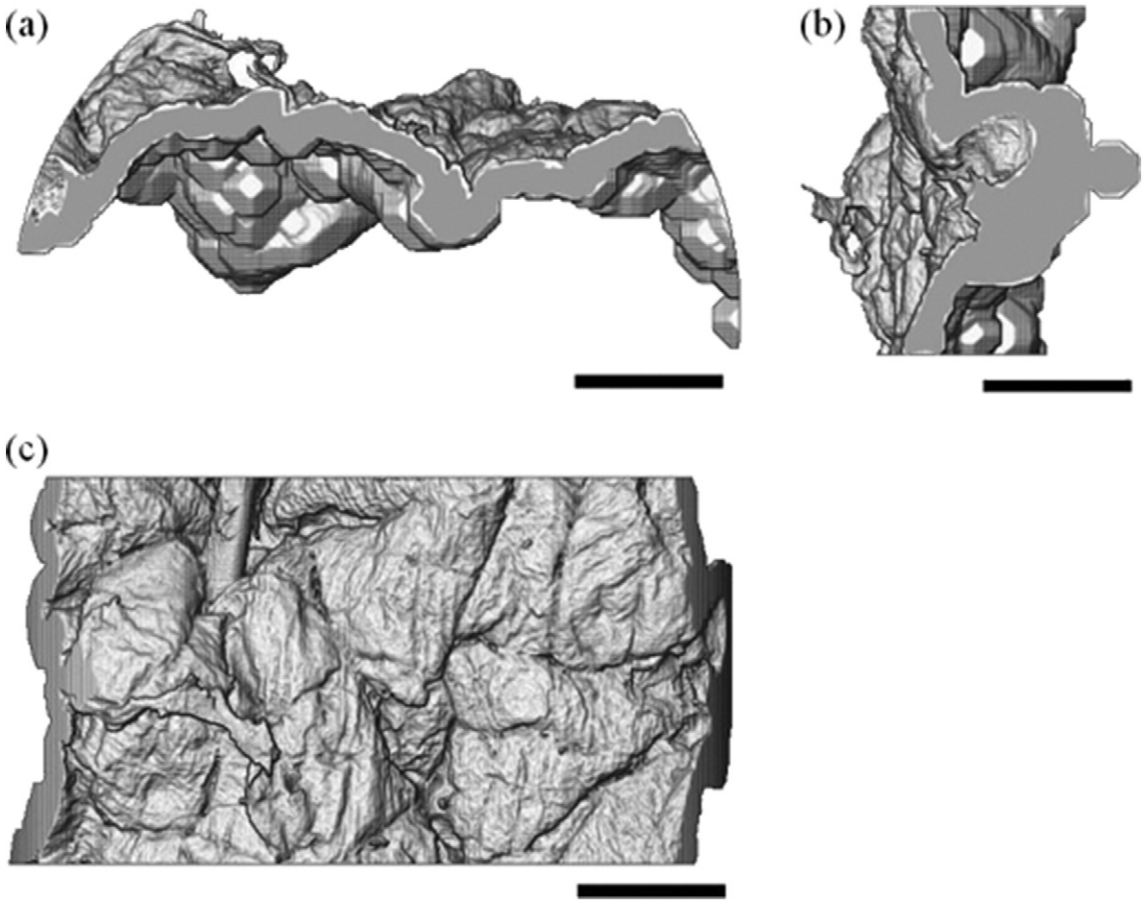

Fig. 10. Volume rendering showing the various orthogonal layouts of the 3D image of the skin, where the (a) XY, (b) XZ and (c) YZ planes are shown. Scale bar represents 100 μm.

of the mechanical properties of subcutaneous tissue on microneedle performance could be investigated.

The relative difference in the elastic modulus between abdominal and back skin was consistent with published data [54]. The storage modulus (elastic properties) was greater than the loss modulus (viscous properties) for both abdominal and back skin. This trends fits a previous study with nanoindentation on murine skin [55].

Elastic modulus values reported by Zak et al. [54] for porcine foetal skin using tensile testing were between 100 and 200 times greater than results obtained in our study with dynamic nanoindentation. Our data better matches in vivo data, for example as reported by Groves [56] and Zahouani et al. [57]. The disparity in mechanical property data reported for various biomechanical studies in the literature highlights complexities due to different tissue types and testing methodologies. Furthermore, Crichton et al. [15] have demonstrated that there is size effect in the micromechanical properties of skin, with the elastic modulus increasing with a decrease in the size of the indenter probe.

A range of different skin types have been used in the literature for microneedle tests in vitro including murine skin, which it has been suggested behaves similar to human skin for microneedle penetration studies [23]. However, the biomechanical behaviour of ex vivo murine skin and human skin is quite different. Under low loads human skin undergoes more extension than murine skin. Also, murine skin is thinner than human skin [58], with a significantly thinner epidermal layer

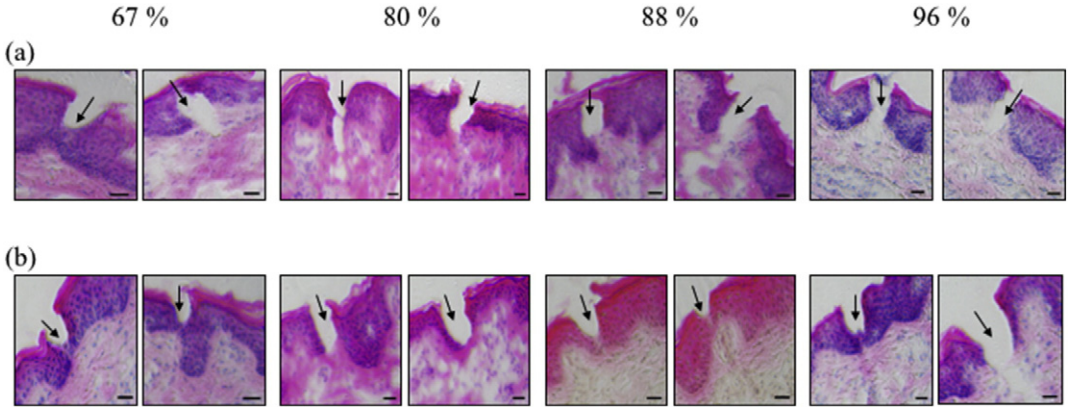

Fig. 11. Example images showing how the various in water content of the subcutaneous mimic affected perforation quality (methylene blue staining) and perforation depth (H&E staining) for (a) abdominal skin and (b) back skin. Scale bar represents 100 μm.

Please cite this article as: K. Moronkeji, et al., The role of subcutaneous tissue stiffness on microneedle performance in a representative in vitro model of skin, J. Control. Release (2016), http://dx.doi.org/10.1016/j.jconrel.2016.11.004

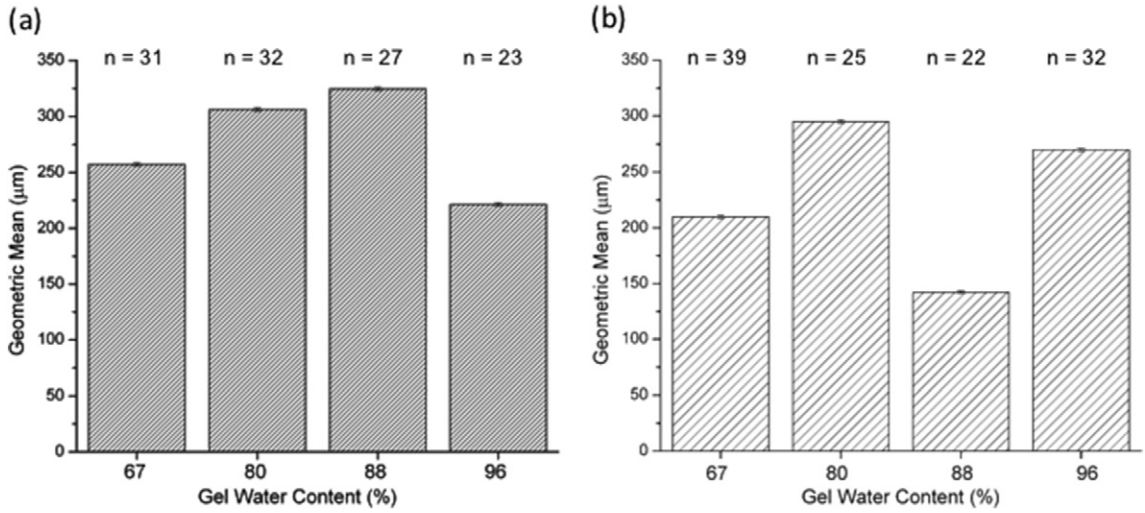

Fig. 12. Perforation depth data (a) Abdominal skin (b) Back skin. Data are presented as geometric mean (geoSD). The number of images in each group (n) are listed above each bar.

[59]. Hence, these issues need to be taken into account when developing a biomechanically representative model of human skin [60].

In our model, we used neonatal porcine skin which exhibits biomechanical properties similar to human skin [28,61]. By selecting skin from two anatomical locations, we were able to vary the skin thickness (≈0.79 mm vs ≈2.43 mm thick in the abdomen and back respectively) in the models and also the skin stiffness. The thicker back skin was approximately twice as stiff (Table 2). The elastic (G′) and viscous component (G″) were both lower for abdominal skin compared to back skin. The depth of penetration was typically lower in the back skin relative to the abdominal skin.

All of our tests were conducted on full thickness skin specimens. The importance of utilising full thickness skin samples for mechanical characterisation was highlighted by Zahouani et al. [57] who showed that the dermis makes a significant contribution to skin because of its load bearing capabilities. Furthermore, it is easier to penetrate the human epidermis without the dermal layer [59], hence tests on isolated layers of skin are not representative of in vivo conditions for microneedle studies.

4.2. Penetration efficiency

Both the methylene blue staining and H&E images show that with the dense arrays used in this study, 100% penetration is not observed. Our findings are in line with those of other researchers who have used less dense arrays [42]. The penetration efficiency determined from methylene blue staining varied from 43 to 93% for the regions analysed. Hence, the expected frequency of microneedle breaches i.e. with clearly visible breaches every 360 μm were not seen in the H&E images. This is likely to be due to the substantial surface topography of skin (as highlighted by the XMT imaging, Fig. 10). Also, there may be unavoidable issues due to the required tissue sectioning and also due to the sectioning process.

4.3. The role of the subcutaneous mimic on microneedle performance

The insertion force (as presented in Fig. 8a), is likely to be the point at which the force exerted on the needles causes piercing of the skin, as described by Olatunji et al. [22]. The value of this force was higher for the stiffer back skin but was not overly influenced by the subcutaneous mimic properties in any of the models. However, when examining the maximum force, it was clear that the subcutaneous layer played an important role in microneedle performance for the abdominal skin models. The maximum force measured by the load cell decreased by approximately 37% from the 67% to the 96% model. Although the penetration efficiency decreased slightly with gel water content, the average depth size and area of breach increased with gel water content. However, with the 96% gel there appeared to be a reduction in these

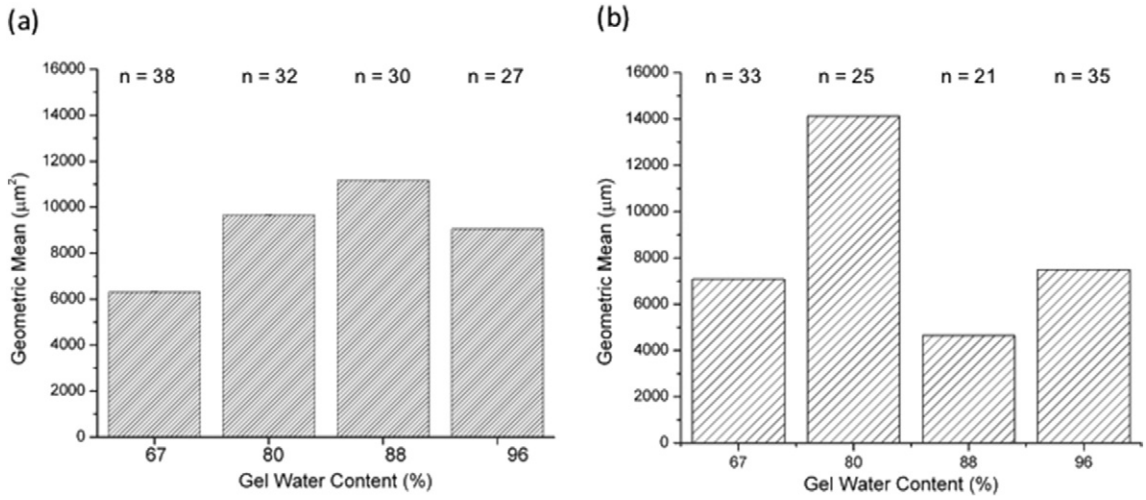

Fig. 13. Breach area (a) Abdominal skin (b) Back skin Data are presented as geometric mean (geoSD). The number of images in each group (n) are listed above each bar.

Please cite this article as: K. Moronkeji, et al., The role of subcutaneous tissue stiffness on microneedle performance in a representative in vitro model of skin, J. Control. Release (2016), http://dx.doi.org/10.1016/j.jconrel.2016.11.004

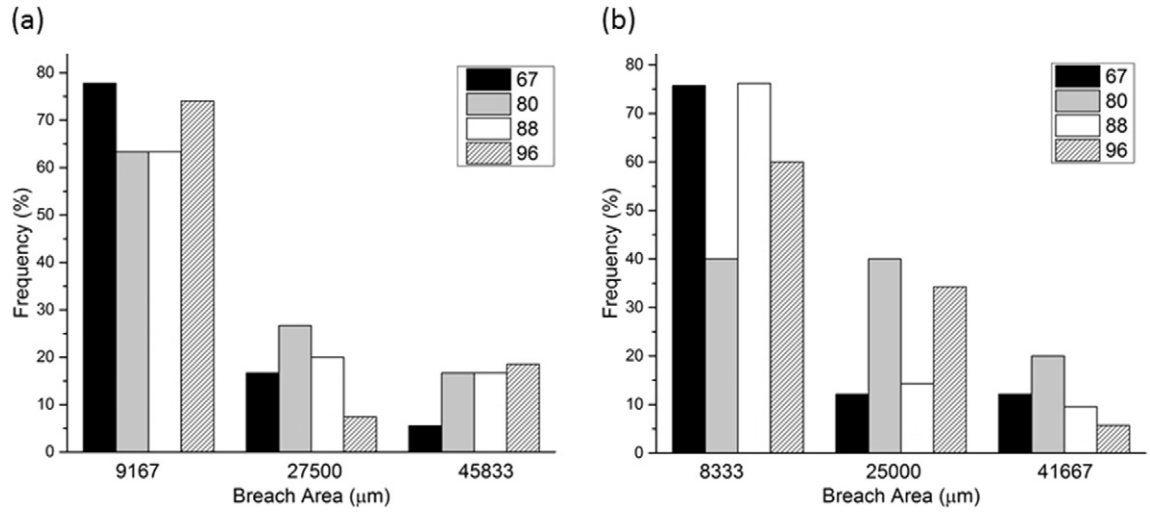

Fig. 14. Histogram distribution of the breach areas, where (a) abdominal skin models and (b) back skin models. The bin centres are marked on the x-axis for the two data sets. The gel water content in the different models are indicated by the histogram legends.

parameters. Although these data suggest that the high compliance of the subcutaneous mimic in this model appears to result in a poorer interaction of the skin with the microneedle array, the histogram data (Fig. 14a) shows that the distribution of small (<10,000 μm) and large breach areas (>20,000 μm) is comparable to the 80% and 88% gels. For the back skin, the maximum force did not decrease as found in the abdominal skin with increasing compliance of the subcutaneous mimic. This is related to the stiffness and thickness of the back skin. The overall trends in depth of microneedle penetration and breach area matched those found in the abdominal skin. The main difference was the average data reported for the 88% model. However, the histogram data for this model (Fig. 14b) also demonstrates that the overall trends are relatively consistent in terms of microneedle performance as compared to gel water content. Some of the disparities may be related to the inherent issues with histological assessment of the microneedle penetration. The disadvantages of histology are that only a small portion of the tissue can be sectioned, which means that useful information is lost with the tissue that is discarded. Furthermore, it involves time-consuming fixing, sectioning and staining steps. Coulman et al. demonstrated that histological measurements of microneedle penetration lead to an overestimation [62,63]. This error is also compounded by the introduction of slight inaccuracies due to skin retraction caused by the removal of the microneedles before staining [64,65]. Despite these limitations, using histology for the light microscopic assessment of skin biopsies is still regarded as the benchmark in dermatology [66,67]. We have attempted to improve on conventional methods of measurement from histological images with our custom image analysis routine. Furthermore, we compared the breach areas determined with H&E staining with XMT images. Although the maximum sample size for the high resolution XMT setup we utilized was 2 × 2 mm, a full 3D dataset was obtained for this volume of tissue. A comparison of 2D XMT slices with the H&E images is shown in the Supplementary Information (Fig. S5). The breach profiles observed with the two techniques appear comparable hence providing validation of the measurements from the H&E images. Further development of the staining and image segmentation methods for soft tissue XMT may make this a powerful technique for microneedle research.

5. Conclusions

In summary, our study demonstrated that the mechanical characteristics of our representative in vitro skin model influenced microneedle performance. We found that by manipulating the fluid content of the subcutaneous layer mimic, the quality of microneedle penetration could be altered. Our findings highlight the importance of conducting in vitro experimentation with more representative skin models and careful consideration of the role of subcutaneous layers on microneedle performance. Our findings have important implications for microneedle application in patients where there is significant change in the compliance of subcutaneous tissue, for example, due to oedema.

Conflict of interest statement

There are no conflicts of interest to declare.

Acknowledgements

The authors thank Dr. Rob Birch and Derek Neary (School of Engineering, University of Liverpool) for assistance with the impact experimental setup, and Mr. Lee Moore (Veterinary Teaching Suite, University of Liverpool) for assistance in sourcing for the suckling pigs. The authors are grateful to the Ali Chirazi (University of Manchester) for assistance with the X-ray CT work at the Henry Moseley X-Ray Imaging Facility. The Henry Moseley X-Ray Imaging Facility has been funded by the Engineering and Physical Sciences Research Council (EPSRC) under Grants EP/M010619, EP/K004530, EP/F007906, and EP/F028431. The work in this study was funded by the Centre for Global Eco-Innovation PhD studentship (Project 106) and Renephra Ltd. The Centre for Global Eco-Innovation was part-funded by the European Regional Development Fund (Grant X02646PR).

Appendix A. Supplementary data

Supplementary data to this article can be found online at http://dx.doi.org/10.1016/j.jconrel.2016.11.004.

References

[1] C. Pegoraro, S. MacNeil, G. Battaglia, Transdermal drug delivery: from micro to Nano, Nanotechnology 4 (2012) 1881–1894.
[2] Y. Lanir, Y.C. Fung, Two-dimensional mechanical properties of rabbit skin. I. Experimental system, J. Biomech. 7 (1974) 29–34.
[3] Y.C. Fung, Biomechanics: Mechanical Properties of Living Tissues, second ed. Springer-Verlag, New York, 1993.
[4] J.C. Barbenel, J.H. Evans, The time-dependent mechanical properties of skin, J. Invest. Dermatol. 69 (1977) 318–320.
[5] P.G. Agache, C. Monneur, J.L. Leveque, J. De Rigal, Mechanical properties and Young's modulus of human skin in vivo, Arch. Dermatol. Res. 269 (1980) 221–232.
[6] F. Khatyr, C. Imberdis, P. Vescovo, D. Varchon, J.M. Lagarde, Model of the viscoelastic behaviour of skin in vivo and study of anisotropy, Skin Res. Technol. 10 (2004) 96–103.

[7] Y. Lanir, Y.C. Fung, Two-dimensional mechanical properties of rabbit skin. II. Experimental results, J. Biomech. 7 (1974) 171–182.
[8] C.W. Oomens, D.H. van Campen, H.J. Grootenboer, A mixture approach to the mechanics of skin, J. Biomech. 20 (1987) 877–885.
[9] C.H. Daly, G.F. Odland, Age-related-changes in the mechanical-properties of human-skin, J. Investig. Dermatol. 73 (1979) 84–87.
[10] J.L. Leveque, J. de Rigal, P.G. Agache, C. Monneur, Influence of ageing on the in vivo extensibility of human skin at a low stress, Arch. Dermatol. Res. 269 (1980) 127–135.
[11] J. Sandby-Moller, T. Poulsen, H.C. Wulf, Epidermal thickness at different body sites: relationship to age, gender, pigmentation, blood content, skin type and smoking habits, Acta Derm. Venereol. 83 (2003) 410–413.
[12] H. Tagami, M. Ohi, K. Iwatsuki, Y. Kanamaru, M. Yamada, B. Ichijo, Evaluation of the skin surface hydration in vivo by electrical measurement, J. Invest. Dermatol. 75 (1980) 500–507.
[13] M.F. Leyva-Mendivil, A. Page, N.W. Bressloff, G. Limbert, A mechanistic insight into the mechanical role of the stratum corneum during stretching and compression of the skin, J. Mech. Behav. Biomed. Mater. 49 (2015) 197–219.
[14] T. Jee, K. Komvopoulos, Skin viscoelasticity studied in vitro by microprobe-based techniques, J. Biomech. 47 (2014) 553–559.
[15] M.L. Crichton, X. Chen, H. Huang, M.A. Kendall, Elastic modulus and viscoelastic properties of full thickness skin characterised at micro scales, Biomaterials 34 (2013) 2087–2097.
[16] R.K. Sivamani, D. Liepmann, H.I. Maibach, Microneedles and transdermal applications, Expert Opin. Drug Deliv. 4 (2007) 19–25.
[17] Y.C. Kim, J.H. Park, M.R. Prausnitz, Microneedles for drug and vaccine delivery, Adv. Drug Deliv. Rev. 64 (2012) 1547–1568.
[18] M.I. Haq, E. Smith, D.N. John, M. Kalavala, C. Edwards, A. Anstey, et al., Clinical administration of microneedles: skin puncture, pain and sensation, Biomed. Microdevices 11 (2009) 35–47.
[19] J. Gupta, H.S. Gill, S.N. Andrews, M.R. Prausnitz, Kinetics of skin resealing after insertion of microneedles in human subjects, J. Control. Release 154 (2011) 148–155.
[20] M.R. Prausnitz, Overcoming skin's barrier: the search for effective and user-friendly drug delivery, Diabetes Technol. Ther. 3 (2001) 233–236.
[21] M.M. Badran, J. Kuntsche, A. Fahr, Skin penetration enhancement by a microneedle device (Dermaroller (R)) in vitro: dependency on needle size and applied formulation, Eur. J. Pharm. Sci. 36 (2009) 511–523.
[22] O. Olatunji, D.B. Das, M.J. Garland, L. Belaid, R.F. Donnelly, Influence of Array interspacing on the force required for successful microneedle skin penetration: theoretical and practical approaches, J. Pharm. Sci. 102 (2013) 1209–1221.
[23] J.S. Kochhar, T. Quek, W.J. Soon, J. Choi, S. Zou, L.F. Kang, Effect of microneedle geometry and supporting substrate on microneedle array penetration into skin, J. Pharm. Sci. 102 (2013) 4100–4108.
[24] J.S. Kochhar, W.J. Goh, S.Y. Chan, L.F. Kang, A simple method of microneedle array fabrication for transdermal drug delivery, Drug Dev. Ind. Pharm. 39 (2013) 299–309.
[25] G.A. Yan, K.S. Warner, J. Zhang, S. Sharma, B.K. Gale, Evaluation needle length and density of microneedle arrays in the pretreatment of skin for transdermal drug delivery, Int. J. Pharm. 391 (2010) 7–12.
[26] J.H. Park, M.G. Allen, M.R. Prausnitz, Biodegradable polymer microneedles: fabrication, mechanics and transdermal drug delivery, J. Control. Release 104 (2005) 51–66.
[27] F.J. Verbaan, S.M. Bal, D.J. van den Berg, W.H.H. Groenink, H. Verpoorten, R. Luttge, et al., Assembled microneedle arrays enhance the transport of compounds varying over a large range of molecular weight across human dermatomed skin, J. Control. Release 117 (2007) 238–245.
[28] O.A. Shergold, N.A. Fleck, D. Radford, The uniaxial stress versus strain response of pig skin and silicone rubber at low and high strain rates, Int. J. Impact Eng. 32 (2006) 1384–1402.
[29] A. Markidou, W.Y. Shih, W.H. Shih, Soft-materials elastic and shear moduli measurement using piezoelectric cantilevers, Rev. Sci. Instrum. 76 (2005).
[30] A. Caron-Laramée, M. Brouillette, Spherical Indentation Testing on Ballistic Gelatin and Perma-Gel, American Society of Mechanical Engineers, ASME 2014 International Mechanical Engineering Congress and Exposition, 2014 (p. V003T03A4-VT03A4).
[31] Z.I. Kalcioglu, M. Qu, K.E. Strawhecker, T. Shazly, E. Edelman, M.R. VanLandingham, et al., Dynamic impact indentation of hydrated biological tissues and tissue surrogate gels, Philos. Mag. 91 (2011) 1339–1355.
[32] P. Moy, M. Foster, C.A. Gunnarsson, T. Weerasooriya, Loading rate effect on tensile failure behavior of gelatins under mode I, Dynamic Behavior of Materials, Volume 1, Springer 2011, pp. 15–23.
[33] Ryckman RA, Powell DA, Lew A. Ballistic penetration of Perma-Gel. Shock Compression of Condensed Matter-2011: Proceedings of the Conference of the American Physical Society Topical Group on Shock Compression of Condensed Matter: AIP Publishing; 2012. p. 143–8.
[34] R. Akhtar, E.R. Draper, D.J. Adams, H. Pfaff, Complex shear modulus of hydrogels using a dynamic nanoindentation method, in: A.S. Tekalur, P. Zavattieri, S.C. Korach (Eds.), Mechanics of Biological Systems and Materials, Volume 6, Springer International Publishing, Cham 2016, pp. 141–145 Proceedings of the 2015 Annual Conference on Experimental and Applied Mechanics.
[35] E.R. Draper, L.L.E. Mears, A.M. Castilla, S.M. King, T.O. McDonald, R. Akhtar, et al., Using the hydrolysis of anhydrides to control gel properties and homogeneity in pH-triggered gelation, RSC Adv. 5 (2015) 95369–95378.
[36] B. Bhushan, W. Tang, S. Ge, Nanomechanical characterization of skin and skin cream, J. Microsc. 240 (2010) 135–144.
[37] K. Moronkeji, S. Todd, I. Dawidowska, R. Akhtar, In Vitro Quantification of Optimal Impact Properties for Microneedle Penetration. Mechanics of Biological Systems and Materials, Volume 6, Springer, 2016 39–49.
[38] L.V. Burgin, R.M. Aspden, A drop tower for controlled impact testing of biological tissues, Med. Eng. Phys. 29 (2007) 525–530.
[39] M.F. Lara, E. Gonzalez-Gonzalez, T.J. Speaker, R.P. Hickerson, D. Leake, L.M. Milstone, et al., Inhibition of CD44 gene expression in human skin models, using self-delivery short interfering RNA administered by dissolvable microneedle arrays, Hum. Gene Ther. 23 (2012) 816–823.
[40] J.D. Bancroft, M. Gamble, Theory and Practice of Histological Techniques: Elsevier Health Sciences, 2008.
[41] G. Li, A. Badkar, S. Nema, C.S. Kolli, A.K. Banga, In vitro transdermal delivery of therapeutic antibodies using maltose microneedles, Int. J. Pharm. 368 (2009) 109–115.
[42] K. van der Maaden, E. Sekerdag, W. Jiskoot, J. Bouwstra, Impact-insertion applicator improves reliability of skin penetration by solid microneedle arrays, AAPS J. 16 (2014) 681–684.
[43] H.K. Graham, R. Akhtar, C. Kridiotis, B. Derby, T. Kundu, A.W. Trafford, et al., Localised micro-mechanical stiffening in the ageing aorta, Mech. Ageing Dev. 132 (2011) 459–467.
[44] S.J. Schambach, S. Bag, L. Schilling, C. Groden, M.A. Brockmann, Application of micro-CT in small animal imaging, Methods 50 (2010) 2–13.
[45] H.R. Buie, G.M. Campbell, R.J. Klinck, J.A. MacNeil, S.K. Boyd, Automatic segmentation of cortical and trabecular compartments based on a dual threshold technique for in vivo micro-CT bone analysis, Bone 41 (2007) 505–515.
[46] E. Pauwels, D. Van Loo, P. Cornillie, L. Brabant, L. Van Hoorebeke, An exploratory study of contrast agents for soft tissue visualization by means of high resolution X-ray computed tomography imaging, J. Microsc. 250 (2013) 21–31.
[47] L.A. Walton, R.S. Bradley, P.J. Withers, V.L. Newton, R.E. Watson, C. Austin, et al., Morphological characterisation of unstained and intact tissue micro-architecture by X-ray computed micro- and nano-tomography, Sci. Report. 5 (2015) 10074.
[48] R. Heilbronner, S. Barrett, Image Analysis in Earth Sciences: Microstructures and Textures of Earth Materials, Springer Science & Business Media, 2013.
[49] M. Geerligs, G.W. Peters, P.A. Ackermans, C.W. Oomens, F.P. Baaijens, Does subcutaneous adipose tissue behave as an (anti-) thixotropic material? J. Biomech. 43 (2010) 1153–1159.
[50] C. Pailler-Mattei, S. Bec, H. Zahouani, In vivo measurements of the elastic mechanical properties of human skin by indentation tests, Med. Eng. Phys. 30 (2008) 599–606.
[51] M. Geerligs, G.W. Peters, P.A. Ackermans, C.W. Oomens, F. Baaijens, Linear viscoelastic behavior of subcutaneous adipose tissue, Biorheology 45 (2008) 677–688.
[52] M. Mridha, S. Odman, Characterization of subcutaneous edema by mechanical impedance measurements, J. Investig. Dermatol. 85 (1985) 575–578.
[53] M. Mridha, S. Odman, P.A. Oberg, Mechanical pulse-wave propagation in gel, normal and edematous tissues, J. Biomech. 25 (1992) 1213–1218.
[54] M. Zak, P. Kuropka, M. Kobielarz, A. Dudek, K. Kaleta-Kuratewicz, S. Szotek, Determination of the mechanical properties of the skin of pig foetuses with respect to its structure, Acta Bioeng. Biomech. 13 (2011) 37–43.
[55] M.A.F. Kendall, Y.F. Chong, A. Cock, The mechanical properties of the skin epidermis in relation to targeted gene and drug delivery, Biomaterials 28 (2007) 4968–4977.
[56] R.B. Groves, Quantifying the Mechanical Properties of Skin in Vivo and Ex Vivo to Optimise Microneedle Device Design, Cardiff University, 2011.
[57] H. Zahouani, C. Pailler-Mattei, B. Sohm, R. Vargiolu, V. Cenizo, R. Debret, Characterization of the mechanical properties of a dermal equivalent compared with human skin in vivo by indentation and static friction tests, Skin Res. Technol. 15 (2009) 68–76.
[58] Z. Ding, F.J. Verbaan, M. Bivas-Benita, L. Bungener, A. Huckriede, D.J. van den Berg, et al., Microneedle arrays for the transcutaneous immunization of diphtheria and influenza in BALB/c mice, J. Control. Release 136 (2009) 71–78.
[59] H. Li, Y.S. Low, H.P. Chong, M.T. Zin, C.Y. Lee, B. Li, et al., Microneedle-mediated delivery of copper peptide through skin, Pharm. Res. 32 (2015) 2678–2689.
[60] R.B. Groves, S.A. Coulman, J.C. Birchall, S.L. Evans, An anisotropic, hyperelastic model for skin: experimental measurements, finite element modelling and identification of parameters for human and murine skin, J. Mech. Behav. Biomed. Mater. 18 (2013) 167–180.
[61] F. Cilurzo, P. Minghetti, C. Sinico, Newborn pig skin as model membrane in in vitro drug permeation studies: a technical note, AAPS PharmSciTech 8 (2007), E94.
[62] J. Birchall, S. Coulman, M. Pearton, C. Allender, K. Brain, A. Anstey, et al., Cutaneous DNA delivery and gene expression in ex vivo human skin explants via wet-etch micro-fabricated micro-needles, J. Drug Target. 13 (2005) 415–421.
[63] S.A. Coulman, J.C. Birchall, A. Alex, M. Pearton, B. Hofer, C. O'Mahony, et al., In vivo, in situ imaging of microneedle insertion into the skin of human volunteers using optical coherence tomography, Pharm. Res. 28 (2011) 66–81.
[64] R.F. Donnelly, M.J. Garland, D.I. Morrow, K. Migalska, T.R. Singh, R. Majithiya, et al., Optical coherence tomography is a valuable tool in the study of the effects of microneedle geometry on skin penetration characteristics and in-skin dissolution, J. Control. Release 147 (2010) 333–341.
[65] E.Z. Loizidou, N.A. Williams, D.A. Barrow, M.J. Eaton, J. McCrory, S.L. Evans, et al., Structural characterisation and transdermal delivery studies on sugar microneedles: experimental and finite element modelling analyses, European Journal of Pharmaceutics and Biopharmaceutics: Official Journal of Arbeitsgemeinschaft fur Pharmazeutische Verfahrenstechnik eV 89 (2015) 224–231.
[66] M.N. Holme, G. Schulz, H. Deyhle, T. Weitkamp, F. Beckmann, J.A. Lobrinus, et al., Complementary X-ray tomography techniques for histology-validated 3D imaging of soft and hard tissues using plaque-containing blood vessels as examples, Nat. Protoc. 9 (2014) 1401–1415.
[67] V.L. Newton, J.C. McConnell, S.A. Hibbert, H.K. Graham, R.E.B. Watson, Skin aging: molecular pathology, dermal remodelling and the imaging revolution, G. Ital. Dermatol. Venereol. 150 (2015) 665–674.

Please cite this article as: K. Moronkeji, et al., The role of subcutaneous tissue stiffness on microneedle performance in a representative in vitro model of skin, J. Control. Release (2016), http://dx.doi.org/10.1016/j.jconrel.2016.11.004